Chinese Chemical Letters 34 (2023) 108156

Contents lists available at ScienceDirect

Chinese Chemical Letters

journal homepage: www.elsevier.com/locate/cclet

Transition metal phosphides: A wonder catalyst for electrocatalytic hydrogen production

Mingxuan Du, Deng Li*, Shengzhong (Frank) Liu, Junqing Yan*

Key Laboratory of Applied Surface and Colloid Chemistry, Ministry of Education, Shaanxi Engineering Lab for Advanced Energy Technology, School of Materials Science and Engineering, Shaanxi Normal University, Xi'an 710119, China

ARTICLE INFO

Article history:
Received 28 October 2022
Revised 30 December 2022
Accepted 19 January 2023
Available online 21 January 2023

Keywords:
Hydrogen evolution reaction
Phosphating
Doping
Morphology
Heterojunction
Defects

ABSTRACT

Hydrogen evolution from water electrolysis has become an important reaction for the green energy revolution. Traditional precious metals and their compounds are excellent catalysts for producing hydrogen; however, their high cost limits their large-scale practical application. Therefore, the development of affordable electrocatalysts to replace these precious metals is important. Transition metal phosphides (TMPs) have shown remarkable performance for hydrogen evolution and garnered considerable interest in the field of electrolysis. Based on the detailed introduction of TMPs in previous studies, we have systematically summarized the preparation methods, improvement methods, and development opportunities of TMPs and proposed "stimulatory factors" as a fundamental factor affecting the performance of TMPs herein. As the core of this research, "stimulatory factors" can provide numerous solutions to improve the performance of TMP materials and provide a good starting point for TMP research.

1. Introduction

With rapid development of human society, an excessive amount of fossil fuels is consumed, causing energy security crisis and environmental pollution. Thus, developing sustainable and environmentally friendly energy sources to gradually replace traditional fossil fuels is crucial. Hydrogen has a high calorific value and produces nonpolluting combustion byproducts. Additionally, it can be produced through a variety of renewable energy sources, such as solar and wind. Consequently, hydrogen is considered an ideal energy carrier to substitute traditional fossil fuels. In this regard, hydrogen evolution reactions (HERs) offer an efficient and feasible method for hydrogen production [1–3].

1.1. HER mechanism

HERs involve the transfer of two electrons. Although the reaction mechanism is essentially identical in acidic and alkaline conditions, protons in an acidic solution are derived from H_3O^+, whereas protons in an alkaline solution are derived from H_2O. The basic reaction is as follows:

Volmer reaction:

$$H_3O^+ + e^- \rightarrow H^* + H_2O \text{ (acidic medium)} \quad (1)$$

$$H_3O^+ + e^- + H^* \rightarrow H_2 + H_2O \text{ (acidic medium)} \quad (2)$$

Heyrovsky reaction:

$$H_2O + e^- \rightarrow H^* + OH^- \text{ (alkaline or neutral medium)} \quad (3)$$

$$H_2O + e^- + H^* \rightarrow H_2 + OH^- \text{ (alkaline or neutral medium)} \quad (4)$$

Tafel reaction:

$$H^* + H^* \rightarrow H_2 \text{ (acidic, alkaline or neutral medium)} \quad (5)$$

In this formula, * represents the reaction site on the catalyst surface. The Volmer reaction is the initial electrochemical reaction step in which hydrated protons combine with electrons to form adsorbed hydrogen atoms (H^*) on the catalyst surface. The Heyrovsky reaction is the subsequent electrochemical desorption step in which the adsorbed hydrogen atoms combine with H_3O^+ or H_2O and accept an electron from the electrode surface to generate hydrogen gas (H_2). This is followed by the Tafel reaction, which is a composite desorption step in which two H^* molecules on the catalyst combine directly to form H_2. Accordingly, HER must include electron transfer and desorption steps. Therefore, there are two fundamental reaction mechanisms for HER: the Volmer-Heyrovsky mechanism and the Volmer-Tafel mechanism. Moreover, analyzing the Tafel slope reveals the electrochemical reaction kinetic process during the actual catalytic reaction.

* Corresponding authors.
E-mail addresses: dengli@snnu.edu.cn (D. Li), junqingyan@snnu.edu.cn (J. Yan).

https://doi.org/10.1016/j.cclet.2023.108156
1001-8417/

Table 1
Features of different preparation methods and performance comparison of prepared HER catalysts.

Preparation methods	Material (representative)	Overpotential (mV) (@10 mA/cm^2)	Tafel slope (mV/dec)	Electrolyte	Ref.	Features
Liquid-phase reaction method	Ni_2P/CNT	124	53	0.5 mol/L H_2SO_4	[10]	Flexible operation
	CoP/Ti	85 (@20 mA/cm^2)	50	0.5 mol/L H_2SO_4	[11]	Controllable sample morphology and
	FeP	100	67	0.5 mol/L H_2SO_4	[12]	structure
Gas-solid reaction method	NISP/NF	68.4	44.6	1 mol/L PBS	[13]	Simple and fast
	N–Co_2P/CC	42	68	1 mol/L PBS	[14]	Maintain the original shape of the sample
	FeCoP/CF	44	92	1 mol/L KOH	[15]	
Electrodeposition method	NiCoP/CNT/NF	69	62	1 mol/L KOH	[16]	Environmentally friendly
	NiCuP/NF	130	42.5	1 mol/L KOH	[17]	Few byproducts
	Co–CoP/NF	35	71	1 mol/L KOH	[18]	Difficult to control the sample morphology
Pyrolysis reduction method	CoMoP/C	122	64.06	0.5 mol/L H_2SO_4	[19]	Wide range of applications
	Ni–FeP/C	72	54	0.5 mol/L H_2SO_4	[20]	Used for doping reactions
	CoP/C	110	51	0.5 mol/L H_2SO_4	[21]	Uniform distribution of elements

In HER, adsorption and desorption of hydrogen atoms on the catalyst surface are two opposing processes. If the adsorption force is considerably weak, it is not conducive to hydrogen generation. Conversely, if it is considerably strong, it is conducive to hydrogen generation but not to its release [4]. Therefore, there must be a balance between adsorption and desorption on the catalyst surface. Catalytic activity is usually measured using the free energy of hydrogen adsorption (ΔG_H), and the ΔG_H of a good catalyst should be close to zero. Additionally, the common metal catalyst ΔG_H has a "volcanic" relation with the catalytic activity [5]. Pt-based noble metals exhibit a suitable ΔG_H and a high reaction rate and catalytic activity in practical catalytic reactions. However, the scarcity and high cost of Pt-based noble metals are the biggest obstacles to their large-scale commercial applications. Therefore, developing a cost-effective, abundant, and stable nonprecious metal catalyst for replacing these precious metals is crucial to the application of electrocatalytic hydrogen production technology [6].

1.2. Introduction to TMPs

Transition metal phosphides (TMPs) have undergone nearly two centuries of development since their discovery and are widely used in numerous fields owing to their excellent mechanical strength, electrical conductivity, and chemical stability. Studies on their crystal structure have shown that TMP crystals comprise prismatic structural units with a triangular prismatic geometry, forming an isotropic crystal structure. This crystal structure tends to have more coordinatively unsaturated atoms on its surface, yielding an increased HER catalytic activity [7].

Because phosphides have a higher electronegativity and can absorb electrons from metal atoms, the P atoms in TMPs are considered to be doped into the transition metals. Thus, in the HER reaction, negatively charged P acts as an active site to capture positively charged protons. Accordingly, the catalytic activity of phosphide can be optimized by increasing the P concentration [8]. However, when the P content is too high, the free electrons in the compound and the conductivity of the catalyst material decrease, yielding a decrease in its catalytic activity. Conversely, the metal (M) is the hydride-accepting center, and the higher the metal content, the greater the stability and electrical conductivity of the compound. However, an excess of metal will affect the ratio of P atoms in TMPs, disrupting the equilibrium between the adsorption and desorption of H atoms on the surface of P atoms. Therefore, controlling the proportion of M−P is an important topic in the study of TMPs [9].

Recently, various methods have been developed to prepare TMP-based electrocatalysts, yielding diverse morphologies, orientations, and compositions. In conjunction with the development of preparation methods, effective material engineering strategies to promote catalytic performance have been summarized herein. Additionally, based on the previous overview of TMPs, we present the preparation methods of commonly used TMP materials, the means to improve the performance of TMPs, and the future development direction of TMPs. At the same time, we propose the concept of "stimulatory factors." These "stimulatory factors," as described in the third section, are the core of this paper and represent a precise and concise summary of the various factors affecting the performance of TMPs. We hope that readers will be able to easily identify the most important "stimulatory factors" so that the research on TMPs will have a clear context.

2. Preparation methods of TMP-based materials

Recently, various methods have been developed for preparing TMP catalysts. Currently, the preparation methods of TMPs mainly include the liquid-phase reaction method, gas-solid reaction method, electrodeposition method, and pyrolysis reduction method. All the methods have common advantages, including low-cost and easily accessible raw materials, thorough phosphating, controllable product morphology, facile operation, and mass production. Herein, we list the findings of some recently published literature and summarize the characteristics of each preparation method for reference (Table 1) [10−21].

3. Material engineering strategies to promote the activities of TMP-based electrocatalysts

The catalytic activity and stability of TMPs are good; however, the overpotential of TMPs at 10 mA/cm^2 frequently exceeds 100 mV. Conversely, the overpotential of noble metal catalysts (Pt, RuO_2, and IrO_2) at 10 mA/cm^2 ranges from 10 mV to 30 mV. Consequently, the performance gap between TMPs and noble metal catalysts is very large. To narrow the performance gap between the two, researchers commonly use heteroatom doping, morphology and structure control, heterojunction, vacancy defect, and crystal phase and crystal plane assistance.

3.1. Heteroatom doping

Heteroatom doping improves the catalytic activity of TMPs by introducing different types of atoms. Doping can be divided into three categories based on the types of heteroatoms: metal atom doping, nonmetal atom doping, and metal-nonmetal atom codoping. Ge *et al.* [22] synthesized Mn-doped CoP catalyst materials and investigated the effect of doping atoms on the performance of the catalyst for hydrogen evolution in both acidic and alkaline electrolytes. CoP was doped with Mn atoms, causing the d-band center of Co atoms to shift in a negative direction, indi-

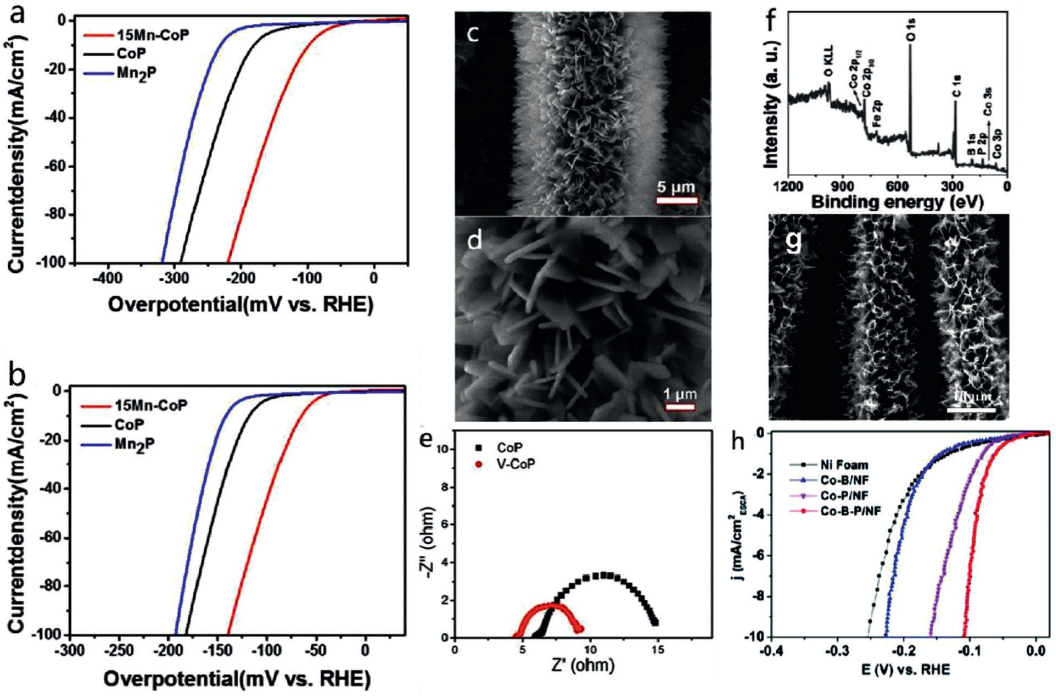

Fig. 1. LSV plots of Mn–CoP, pristine CoP and Mn_2P tested in 1 mol/L KOH (a) and 0.5 mol/L H_2SO_4 (b). Copied with permission [22]. Copyright 2018, American Chemical Society. SEM images of CoMOF (c, d) and V–CoP/CC *vs.* CoP energy Stratgram (e). Copied with permission [23]. Copyright 2020, Frontiers in Chemistry. XPS survey spectrum for Fe–CoP (f). Copied with permission [24]. Copyright 2017, Wiley-VCH. SEM images of W–CoP NAs/CC (g). Copied with permission [25]. Copyright 2019, Wiley-VCH. Comparison of LSV test results of Co–B–P and other samples (h). Copied with permission [27]. Copyright 2018, Royal Society of Chemistry.

cating that the interaction between Co sites and hydrogen may be weakened. In addition, the electrochemical performance of the as-prepared Mn–CoP showed that the overpotentials required to achieve a current density of 10 mA/cm^2 in 0.5 mol/L H_2SO_4 and 1 mol/L KOH are 65 and 100 mV, respectively (Figs. 1a and b). Hua *et al.* [23] synthesized V-doped CoP rice flake arrays (V–CoP/CC) supported on a carbon cloth using a facile water bath/phosphating method, as shown in Figs. 1c and d. V-doped CoP can optimize the electronic structure and enhance the electron transport efficiency in the catalyst. Accordingly, the V–CoP/CC electrode exhibited excellent HER electrocatalytic activity in 1 mol/L KOH solution. Fig. 1e shows the impedance test result for V–CoP/CC *versus* CoP. An overpotential of 98 mV is required to achieve a current density of 10 mA/cm^2. Ma *et al.* [24] synthesized Fe-doped CoP nanoarrays (Fe–CoP/CC) using a carbon cloth as a substrate (Fig. 1f). The LSV test in 0.1 mol/L potassium borate (pH 9.2) required an overpotential of 175 mV to achieve a current density of 10 mA/cm^2, demonstrating excellent HER catalytic performance. In addition, the two-electrode water electrolyzer comprising Fe–Co–Pi–Bi/CC as the anode and FeCoP/CC as the cathode demonstrated a current density of 10 mA/cm^2 at a voltage of 1.95 V. Wang *et al.* [25] prepared W-doped CoP nanosheet arrays (W–CoPNAs/CC) supported on a carbon cloth. Fig. 1g shows that W–CoPNAs/CC exhibits a hierarchical porous structure. The LSV testing of W–CoPNAs/CC in acidic, alkaline, and neutral electrolytes showed that overpotentials of 89, 94, and 102 mV, respectively, were required to achieve a current density of 10 mA/cm^2, confirming an excellent catalytic performance. Because of the porous nature of the arrays of W-doped CoP nanosheets, the number of active sites increased and the catalytic performance improved. Wang *et al.* [26] synthesized N–CoP_2 nanowires supported on a carbon cloth using simple hydrothermal, thermal phosphating, and ammonia atmosphere calcination methods. Further, they tested the HER performance in 0.5 mol/L H_2SO_4; the overpotential required to reach a current density of 10 mA/cm^2 was 38 mV, which is considerably lower than that of undoped CoP (125 mV). This performance improvement is attributed to the CoP_2 lattice shrinkage and ΔG_{H^*} reduction caused by N doping. Sun *et al.* [27] prepared an amorphous B-doped CoP ternary alloy $Co_{2.90}B_{0.73}P_{0.27}$ supported on nickel foam *via* an ultrasonic method, which has an excellent catalytic performance in alkaline electrolytes. Accordingly, the overpotential required to reach a current density of 10 mA/cm^2 was 12 mV (Fig. 1h), the Tafel slope was as low as 42.1 mV/dec, and the stability was maintained for 20 h at a high current density of 1 A/cm^2, even surpassing that of commercial Pt/C. This excellent performance is attributed to the synergistic effect of B and P, which weakens the hydrogen adsorption on the surface and inhibits the oxidation of Co.

In Section 3.1 on heteroatom doping, we can conclude that the introduction of heteroatoms destroys the periodicity of the TMP lattice, modifies the local electronic structure, shifts the *d*-electron center away from the Fermi level, and lowers the reaction energy barrier, accelerating the reaction kinetics [28,29]. By doping atoms with high electrical conductivity with TMPs, the electrical conductivity and electrocatalytic performance of the material can be improved. Additionally, this results in a synergistic effect between the substrate and active components, which enhances the stability of TMP particles and reduces the agglomeration phenomenon to a certain extent [30–32].

3.2. Morphology and structure control

In the HER reaction, the structure of the electrode has a considerable impact on the progression of the catalytic reaction. The electrode structure determines the number of available active sites. It also affects mass transport, concentration gradients, and stability. To maximize the catalytic activity of TMPs, researchers frequently start from the nanostructure and components of the catalyst simultaneously and endow the prepared products with particular shapes or large dimensions. A rational design and regulation of morphology and structure can effectively enhance the activity and stability

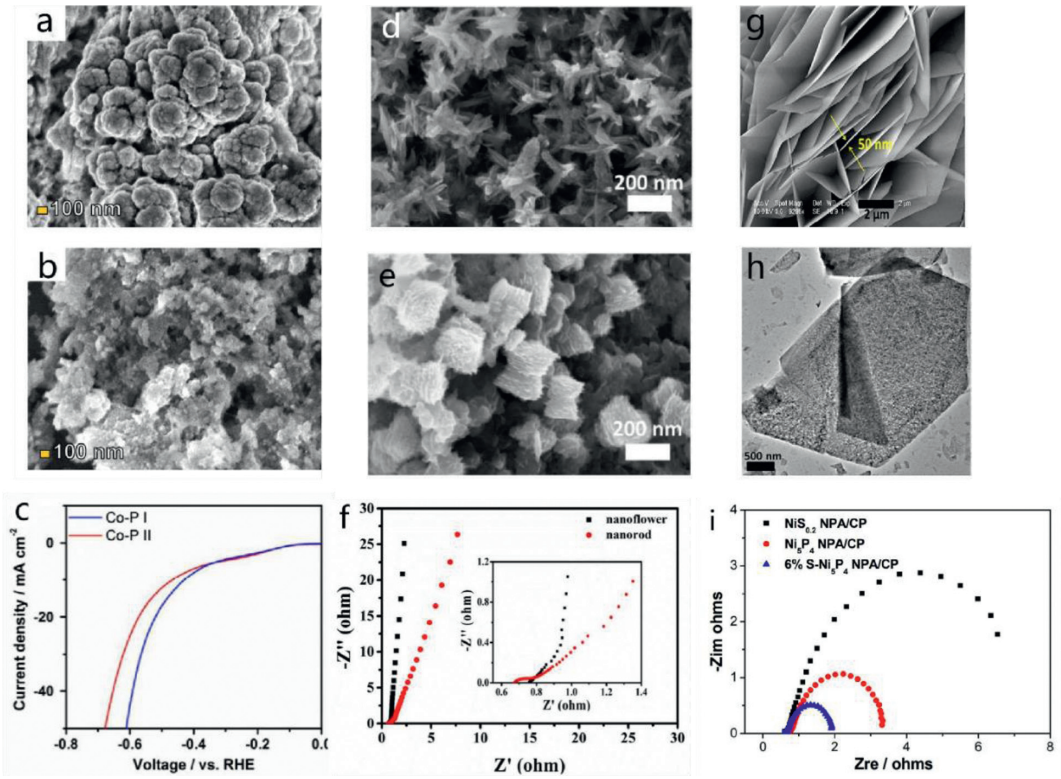

Fig. 2. SEM image of (a) as-synthesized Co–P I and of (b) as-synthesized Co–P II, HER performance of Co–P I and Co–P II in 0.2 mol/L phosphate buffer solution (c). Copied with permission [33]. Copyright 2018, American Chemical Society. SEM images of the Co_2P nanoflowers electrode (d) and Co_2P nanorods electrode (e), Nyquist plots for Co_2P nanorods and Co_2P nanoflowers electrodes at open circuit potential (f). Copied with permission [35]. Copyright 2016, American Chemical Society. Structural characterizations of the 6% S–Ni_5P_4NPA/CP, SEM image (g) and TEM image (h), Nyquist plots of Ni_5P_4NPA/CP and S–Ni_5P_4NPA/CP (i). Copied with permission [41]. Copyright 2018, American Chemical Society.

of the catalyst. Sumboja *et al.* [33] used $C_4H_6CoO_4$ and $C_{15}H_{21}CoO_6$ as precursors to produce nanostructured cobalt phosphide (Co–P I) and nanoparticle cobalt phosphide (Co–P II) *via* the gas-solid phosphating method. Figs. 2a and b show that both Co–P I and Co–P II have alveolar sac-like structures. Additionally, the LSV test demonstrates the superior catalytic activity of Co–P I (Fig. 2c). Moreover, the special alveolar sac-like nanostructures increase the catalytically active surface area, affording increased HER activity. Yang *et al.* [34] developed CoP nanocrystals with a unique sea urchin-like structure by phosphating at low temperatures. The LSV test was conducted in an acidic medium. When the current density was 100 mA/cm^2, the overpotential was 180 mV. Chen *et al.* [35] used PPh_3 as the phosphorus source to synthesize rod-like and flower-like Co_2P by controlling the phosphating process (Figs. 2d and e). These Co_2P structures exhibit high porosity and specific surface area. Both rod- and flower-shaped Co_2P have low impedances in the EIS test (Fig. 2f). Liu and Li [36] described a new type of CoP hollow polyhedral catalyst in which MOF materials were used as a template and the hollow polyhedral CoP catalyst was successfully prepared *in situ*. This unique structure of CoP increases its specific surface area and porosity, affording a large number of active sites. Through the LSV test of the HER reaction in an alkaline medium, the required overpotential to achieve a current density of 10 mA/cm^2 is 159 mV, and the Tafel slope is 57 mV/dec. Su *et al.* [37] reconstructed the surface structure of CoP and attained stable $Co(OH)_x$@CoP hybridization using an *in situ* electrochemical activation method. $Co(OH)_x$ formed *in situ* accelerates the dissociation of water, yielding a large number of hydrogen atoms, which are transferred to nearby exposed Co active sites to form Co–H bonds. The results of testing the electrocatalytic activity of CoP and $Co(OH)_x$@CoP for HER in 1 mol/L KOH electrolyte indicate that the overpotential required for CoP to reach a current density of 10 mA/cm^2 is 180 mV, whereas the overpotential required for $Co(OH)_x$@CoP is only 100 mV. This enhanced HER activity is attributed to the synergistic effect of the optimized surface/interface of the formed mixed $Co(OH)_x$@CoP species, which increases the concentration of surface hydroxyl groups and promotes water splitting.

In addition, modifying the structure of TMPs can alter the spatial dimensions of the materials, altering the charge distribution and inducing local electric fields [38–40]. Compared with traditional one-dimensional and two-dimensional materials, three-dimensional (3D) materials exhibit superior electron transport capacity and a larger specific surface area, which can increase the probability of the active material reacting with the electrolyte and thus improve the catalytic activity. Therefore, 3D materials have gradually become the mainstream of designing material structures. Chang *et al.* [41] used carbon paper as a substrate to grow S–Ni_5P_4NPA/CP nanoplate arrays with 3D structures (Figs. 2g and h). The 3D-structured S–Ni_5P_4NPA/CP nanoplate arrays exhibit a larger specific surface area and more active sites than nickel phosphide and nickel sulfide. After the LSV testing of HER performance, when the current density reaches 10 mA/cm^2 and 100 mA/cm^2, the overpotential is 56 mV and 104 mV, respectively, while the Tafel slope is only 43.6 mV/dec. S–Ni_5P_4NPA/CP has a lower impedance than Ni_5P_4NPA/CP after EIS testing (Fig. 2i). Wei *et al.* [42] reported a facile method of synthesis using algal bioprecursors to embed NiCoP nanoparticles on graphene aerogels (NiCoP–NPs@GA) using a phosphating step. In 0.5 mol/L H_2SO_4, the overpotential required to achieve a current density of 10 mA/cm^2 is 109 mV, and the Tafel slope is 63 mV/dec. In addition, the large number of pores in the 3D GA matrix effectively prevented the volume expansion and aggregation of NiCoP–NPs, affording its excellent catalytic performance. Yang *et al.* [43] reported that CoP nanoparticles were

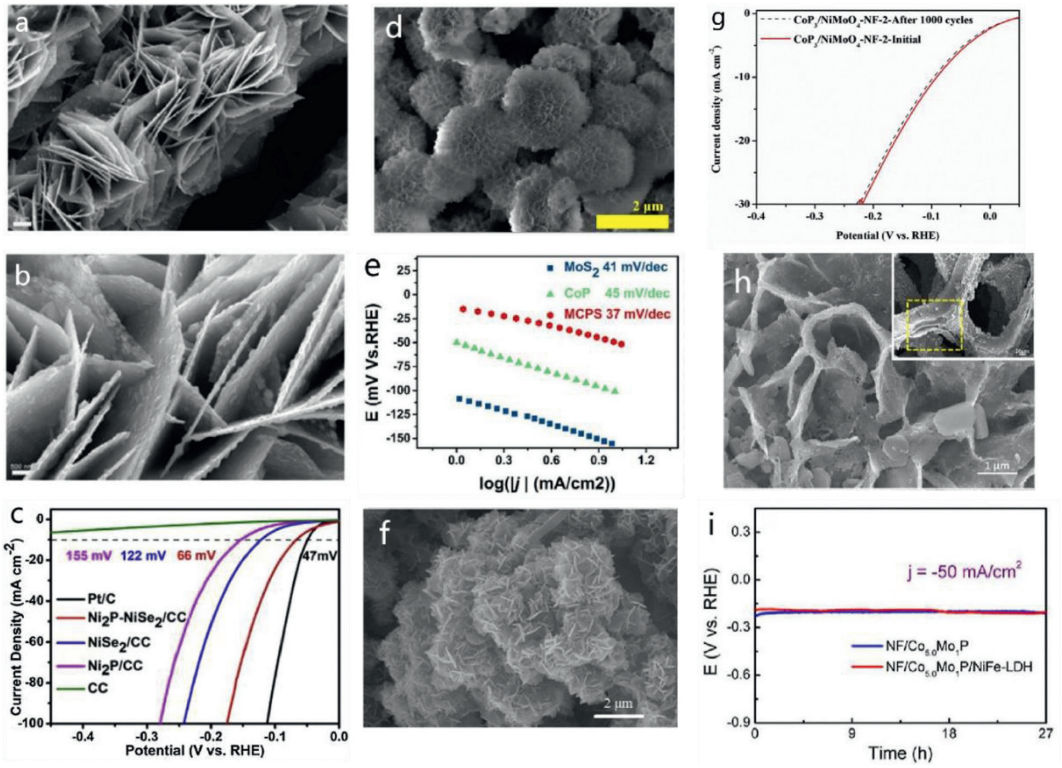

Fig. 3. (a, b) SEM images of Ni_2P–$NiSe_2$/CC at different magnifications and (c) LSV curves of CC, $NiSe_2$/CC, Ni_2P/CC, Ni_2P–$NiSe_2$/CC, and Pt/C at a scan rate of 5 mV/s for the HER in 1 mol/L KOH. Copied with permission [44]. Copyright 2019, Elsevier B.V. (d) SEM image patterns of MoS nanosheet and corresponding Tafel slopes in 0.5 mol/L H_2SO_4 (e). Copied with permission [46]. Copyright 2019, American Chemical Society. SEM images of CoP_3/$NiMoO_4$–NF–1 (f) and polarization curves for CoP_3/$NiMoO_4$–NF–2 before and after 1000 CV sweeps between −0.24 and 0.26 V *vs.* RHE in 1 mol/L KOH (g). Copied with permission [48]. Copyright 2019, Elsevier Ltd. SEM images for $Co_{5.0}Mo_1P$/NiFe–LDH (h) and stability test of $Co_{5.0}Mo_1P$/NiFe–LDH and various control samples (i). Copied with permission [50]. Copyright 2020, American Chemical Society.

encapsulated in three-dimensional nitrogen-doped porous carbon (CoP@3D–NPC) catalysts. The unique 3D porous carbon could provide multidimensional electron/ion transport paths to reduce diffusion distances and the encapsulated CoP nanoparticles could prevent it from directly contacting the electrolyte to ensure interfacial stability. Further, they could exhibit outstanding hydrogen evolution catalytic performance in 0.5 mol/L H_2SO_4 and 1 mol/L KOH, and the overpotentials required to obtain a current density of 10 mA/cm^2 were 127 and 203 mV, respectively, while the corresponding Tafel slopes were 58 and 65 mV/dec, respectively.

In Section 3.2 on the regulation of topography, we can conclude that the objective of designing a specific topography is to increase the specific surface area. An increase in specific surface area increases the contact area between the catalyst and the electrolyte, which yields more active sites and the intermediates produced by HER have a greater chance of adsorbing onto the active substances. The multidimensional structure can accelerate the flow of electrolytes and facilitate the transport of substances. These characteristics are important to achieve hydrogen evolution activity and stability.

3.3. Heterojunction effect

A heterostructure is a composite material in which different catalyst materials come into contact to form a heterogeneous interface. Owing to the direct physical contact between each component or phase, the corresponding physicochemical properties of the interface are highly different from those of the bulk phase. Furthermore, these hybrid catalysts generally exhibit strong interfacial interactions. Generally, the rational design of multicomponent heterogeneous structures is crucial in the production of electrocatalysts with considerably enhanced electrocatalytic activity. In the experiments, TMPs can be combined with other substances possessing catalytic properties, and the structure-activity relationship between the heterostructure and catalytic activity enables the enhancement of the catalytic activity. Liu *et al.* [44] synthesized a novel self-supporting Ni_2P–$NiSe_2$/CC heterostructure catalyst with a unique sheet-like structure (Figs. 3a and b). Accordingly, the effect of the catalyst on HER catalytic activity was tested under an alkaline condition of 1 mol/L KOH. An overpotential of 66 mV was observed under a current density of 10 mA/cm^2 (Fig. 3c), and the stability and durability of Ni_2P–$NiSe_2$/CC were found to be excellent. According to calculations using the density functional theory, Ni_2P and $NiSe_2$ exhibit a strong electronic interaction, which optimizes the Gibbs free energy of H/H_2O adsorption and improves the HER activity. Boppella *et al.* [45] synthesized CoP/NiCoP composite nanosheets with a two-dimensional structure. Their NiCoP (111) and CoP (112) planes exhibit interplanar spacings of 0.22 and 0.19 nm, respectively. The well-defined lattice fringes demonstrate the formation of nanoheterojunctions between CoP/NiCoPs, and the coupling effect at the phase interface improves the HER reaction kinetics, optimizing the HER catalytic performance. Ge *et al.* [46] reported the use of two-dimensional zeolite imidazole framework arrays as templates to combine MoS_2 nanosheets with CoP for HER reaction; Fig. 3d shows its structure. In 0.5 mol/L H_2SO_4 and 1 mol/L KOH, a current density of 10 mA/cm^2 required overpotentials of 53 and 77 mV, respectively. Moreover, the Tafel slope reached 37 mV/dec in an electrolyte containing 0.5 mol/L of H_2SO_4, (Fig. 3e). Pan *et al.* [47] constructed a novel, highly active CoP/MoS_2–CNTs heterostructure catalyst *via* the *in situ* growth of CoP on the surface of MoS_2 and CNTs. The electrocatalytic performance of HER in 0.5 mol/L H_2SO_4 was excellent. Accordingly, only a 10 mV overcharge was required to obtain an overpotential of 10 mA/cm^2, and the Tafel slope was found to be

42 mV/dec. The results show that the electrocatalytic activity of the CoP/MoS_2 composite catalyst is superior to that of CoP and MoS_2 owing to a strong synergistic effect. Wang *et al.* [48] synthesized CoP_3/$NiMoO_4$ nanosheets (CoP_3/$NiMoO_4$–NF) *in situ* on nickel foam *via* hydrothermal treatment, annealing, and phosphating (Fig. 3f). The synergistic effect of CoP_3 and $NiMoO_4$ considerably promoted the activity of HER. Furthermore, the nickel foam promotes the vertical growth of well-aligned nanosheet arrays, exposing an increased number of HER active centers. To achieve a current density of 10 mA/cm^2 in 1 mol/L KOH, a HER overpotential of 92 mV was required, with a Tafel slope of 50.7 mV/dec (Fig. 3g). In particular, CoP_3/$NiMoO_4$–NF demonstrated excellent durability, and the electrochemical activity could be maintained for more than 12 h. Wu *et al.* [49] designed a low-cost, high-performance bifunctional electrocatalyst. Heterogeneous Ni_2P–Fe_2P microflakes were synthesized by directly soaking nickel foam in hydrochloric acid and ferric nitrate solution, followed by phosphating, and the catalytic performance of HER under alkaline conditions was enhanced through Ni_2P–Fe_2P heterojunction. The experimental results show that in 1 mol/L KOH fresh water solution, only 168 mV and 186 mV overpotentials were required to achieve current densities of 100 mA/cm^2 and 500 mA/cm^2, respectively. In addition, the hydrophilic nature of the Ni_2P–Fe_2P heterojunction structure was able to provide sufficient space for the diffusion of the electrolyte, enhancing the gas mass transfer rate and affording its outstanding catalytic activity at a high current density. Accordingly, a versatile and cost-effective method for the preparation of heterogeneous metal phosphide catalysts was realized. Mai *et al.* [50] designed a two-dimensional (2D) heterostructured bimetallic phosphide and layered double hydroxide (LDH)-based electrode assembly (Co_xMo_1P/NiFe–LDH) by hydrothermal synthesis. The $Co_{5.0}Mo_1P$/NiFe–LDH hybrid catalyst was obtained through the chemical electrodeposition process (Fig. 3h). According to electrochemical tests, $Co_{5.0}Mo_1P$/NiFe–LDH exhibits excellent HER catalytic performance in 1 mol/L KOH, requiring only 98.9 mV of overpotential to reach a current density of 10 mA/cm^2. The $Co_{5.0}Mo_1P$/NiFe–LDH hybrid catalyst was used as the cathode to achieve a current density of 50 mA/cm^2 at a potential of 1.68 V, and the electrochemical activity could be maintained for 27 h, demonstrating excellent catalytic activity and stability. Additionally, the stability of $Co_{5.0}Mo_1P$/NiFe–LDH was exceptional (Fig. 3i). Yu *et al.* [51] successfully prepared N-doped carbon-coated CoP(MoP)–$CoMoO_3$ heterostructure catalysts [CoP(MoP)–CoMoO@CN] *via* thermal decomposition and phosphating strategies; these catalysts demonstrated excellent performance in 1 mol/L KOH alkaline medium. For the excellent catalytic performance of total water splitting, the HER of CoP(MoP)–CoMoO@CN nanocomposites required an overpotential of 198 mV to achieve a current density of 10 mA/cm^2, and the corresponding Tafel slopes were 95 mV/dec. Importantly, the use of the as-prepared CoP(MoP)–CoMoO@CN heterostructure catalyst as cathode and anode, respectively, yielded a current density of 10 mA/cm^2 at a potential of 1.55 V. The catalyst provides abundant active sites for the HER. This remarkable heterostructured CoP(MoP)–CoMoO@CN catalyst exhibits excellent catalytic activity.

In Section 3.3 on heterojunction, the mechanism of the heterojunction effect is summarized as follows. After the formation of the heterointerface, the periodicity of the metal phosphide lattice is destroyed, affording a change in the local electronic structure. Electronic interactions between species redistribute the electronic densities of their respective states. The modified electronic structure increases the conductivity of the system and accelerates charge transfer, accelerating the adsorption/desorption of intermediates and enhancing the reaction kinetics and catalytic activity [52–55].

3.4. Effect of vacancy defect

The vacancy defect refers to the space left in the TMPs catalyst crystal when atoms or ions leave the lattice. Introducing vacancy defects is an effective method for regulating the catalytic performance of TMPs. Zhang *et al.* [56] synthesized Ni_2P nanosheet arrays (V–Ni_2P/NF) with abundant cation vacancy defects through a multi-step reaction process (Fig. 4a). Density functional theory (DFT) calculations proved that the Ni vacancy defect changed the electronic structure near the atoms in the compound, bringing the adsorption energy of H on the surface of the V–Ni_2P/NF catalyst closer to zero and thereby decreasing the catalyst energy. The potential barriers and cation vacancies for the HER pushed the *d*-band center of the catalyst away from the Fermi level. The electrocatalytic performance of Ni_2P was successfully optimized viaby cation vacancy engineering, and the V–Ni_2P/NF catalyst was used in HER with good electrocatalytic performance under alkaline conditions, requiring an overpotential of 55 mV to achieve a current density of 10 mA/cm^2 (Fig. 4b). Kwong *et al.* [57] introduced Fe vacancy defects to tune the electronic structure of iron phosphide (FeP), where Mg was introduced as a sacrifice to form a Vc–

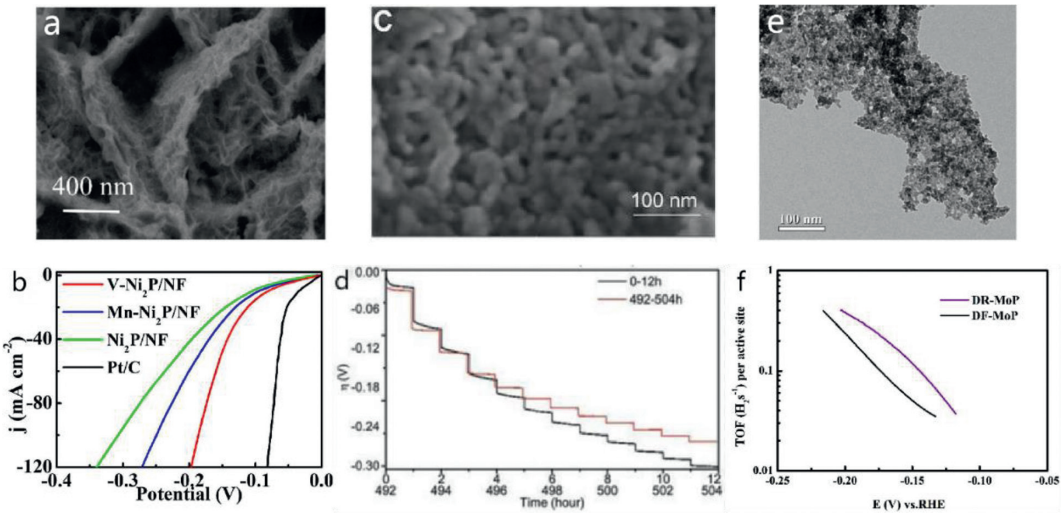

Fig. 4. SEM images of V–Ni_2P/NF (a) and HER performance of as-prepared electrode in 1 mol/L KOH (b). Copied with permission [56]. Copyright 2019, Elsevier. SEM image of V–$Ni_{12}P_5$ (c) and chronoamperometry test up to 504 h without iR correction (d). Copied with permission [58]. Copyright 2020, Wiley-VCH. TEM images of DR-MoP (e) and TOF values of DR-MoP and DF-MoP (f). Copied with permission [59]. Copyright 2018, Elsevier Ltd.

FeP film. Vc–FeP had a higher phosphorus content than FeP and Mg–FeP, and the higher phosphorus content afforded more negative charges, which attracted more protons and enhanced the hydrogen evolution activity. In 1 mol/L KOH and 0.5 mol/L H_2SO_4, the overpotentials required to achieve a current density of 10 mA/cm^2 were 108 and 65 mV, respectively, and the Faradaic efficiency was close to 100%. Theoretical and experimental analysis showed that the HER activity of the enhanced catalyst resulted from the presence of iron vacancies, which optimized the electronic structure of the catalyst and brought the hydrogen adsorption-free energy close to zero, thereby enhancing the catalytic performance of the catalyst. Duan *et al*. [58] prepared (V–$Ni_{12}P_5$) with P vacancy defects using nickel foam as thea substrate. Fig. 4c depicts its structure. According to DFT calculations, a considerable number of electrons were accumulated in V–$Ni_{12}P_5$, which redistributed the electrons in the Ni_2P crystal and enhanced the catalytic activity of HER. The LSV test for the HER reaction of V–$Ni_{12}P_5$, in 1 mol/L KOH solution, yielded a current density of 10 mA/cm^2, requiring an overpotential of 27.7 mV, with a Tafel slope of only 30.88 mV/dec. Additionally, the stability of the catalyst was observed to be excellent after extensive testing (Fig. 4d). Zhang [59] and other research groups synthesized defect-rich structural DR-MoP catalysts through a novel and simple low-temperature calcination strategy (Fig. 4e). It is a three-pronged approach: (1) When the synthesis temperature is low, the grain growth is inhibited, the grain size becomes smaller, and the grain boundary widens; (2) Sodium hypophosphite is decomposed into PH_3, which will help aids the formation of a porous structure with manymore exposed areas; and (3) a lower synthesis temperature will lead tocauses an insufficient reaction, resulting inyielding residual Mo–O bonds of the precursor, allowing oxygen incorporation. By evaluating the performance of DR-MoP, it has been demonstrated that introducing defects into the crystal *via* the aforementioned method can provide manymore active sites, and that doping with O atoms can increase the intrinsic conductivity. When applied to the HER reaction, the DR-MoP catalyst demonstrated excellent catalytic activity and stability in both acidic and alkaline electrolytes, with required overpotentials of 156 and 104 mV at a current density of 10 mA/cm^2, corresponding to Tafel slopes of 49 and 50 mV/dec (Fig. 4f), respectively. DFT analysis revealed that the introduction of P vacancy defects reduced the degree of hybridization of M (transition metal) 3d and 2p orbitals and considerably increased the electron density of M and P atoms near the P vacancy [60–62].

In Section 3.4 on vacancy defects, the introduction of vacancy defects in TMPs alters its local atomic structure and coordination number and also increases the number of catalytically active sites. Additionally, vacancy defects modify the local atomic structure, yielding modifications to the electronic structure, which causes the d-band center to move away from the Fermi level and reduces the adsorption energy of hydrogen on the catalyst surface [63,64]. Simultaneously, the active site is increased and the HER reaction energy barrier is lowered.

3.5. Effect of crystal phase/crystal plane

Controlling the crystalline phase of TMPs (single-crystalline phase, amorphous phase, and polycrystalline metal phosphide with element doping) is also essential to optimize the activity of the catalyst. Li *et al*. [65] reported a new gas-solid synthesis method to synthesize single-crystal cobalt phosphide nanowires (CoP NWs) on porous Co foams. According to the TEM image shown in Fig. 5a, the interplanar spacing comprises the well-resolved lattice fringes at 0.254 nm, demonstrating the (200) plane of orthorhombic CoP. The corresponding fast Fourier transform (FFT) patterns of these CoP NWs reveal their single-crystal nature to further analyze their electrochemical performance. In 1 mol/L KOH, the HER

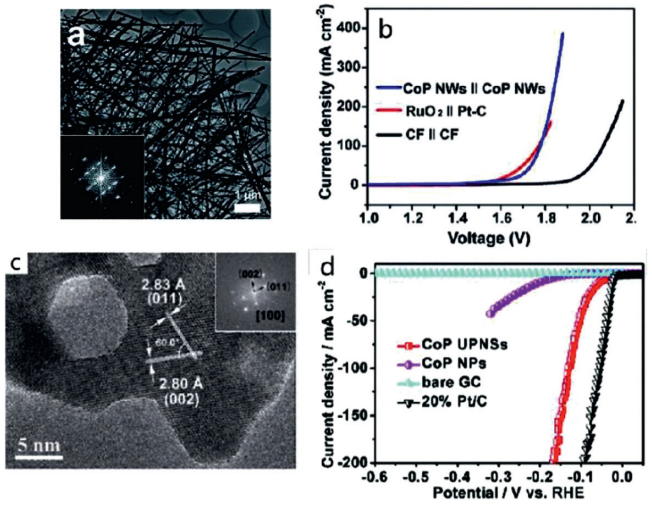

Fig. 5. TEM image of CoP NWs (a), the corresponding fast Fourier transformation (FFT) pattern of this CoP NW (inset of a) and overall water splitting performance of the two-electrode electrolyzers (b). Copied with permission [65]. Copyright 2017, Royal Society of Chemistry. HRTEM images and the associated FFT pattern (inset c) of CoP UPNSs (c) and *I-R* corrected polarization curves of CoP UPNSs, CoP NPs, bare GC, and 20% Pt/C (d). Copied with permission [67]. Copyright 2017, Royal Society of Chemistry.

requires an overpotential of 244 mV to achieve a current density of 100 mA/cm^2. Additionally, CoP NWs were used as the cathode and anode for water electrolysis, with the overpotentials required to achieve current densities of 10 and 100 mA/cm^2 being 156 and 178 mV, respectively (Fig. 5b), and the CoP NWs catalyst exhibiting excellent catalytic performance. Phosphides with different metal/phosphorus stoichiometric ratios have different intrinsic activities owing to their distinct crystal structures. Their disordered domains contain numerous defects and vacancies, which are considered electrocatalytically active centers. Zhang *et al*. [66] synthesized single-crystal $(Fe_xNi_{1-x})_2P$ nanosheets supported on nickel foam with exposed $\{01\bar{1}\bar{1}\}$ planes. Compared to pristine amorphous Ni_2P, $(Fe_xNi_{1-x})_2P$ nanosheets exhibited superior HER activity. The required overpotentials to achieve a current density of 10 mA/cm^2 in acidic, neutral, and alkaline media, were 81, 90, and 103 mV, respectively. According to the DFT calculations, the $\{01\bar{1}\bar{1}\}$ plane has great charge accumulation around the P active site, which reduces ΔG_{H^*} and ΔG_{H_2O} and enhances catalytic activity.

Different crystal plane indices in the catalyst have different effects on catalytic performance, and the atomic structure of the crystal plane partially determines the interaction strength between the crystal plane and the reactants or intermediates. The geometric and electronic structures of different crystal planes of different catalysts are distinct, yielding distinctive physicochemical properties. Zhang *et al*. [67] prepared ultrathin porous CoP nanosheets in the form of single crystals with exposed {200} crystal faces using a chemical transformation strategy (Fig. 5c). The ultrathin porous CoP nanosheet catalyst exhibits excellent electrochemical HER performance in acidic electrolysis, where overpotentials of 56 and 131 mV are required to obtain current densities of 10 and 100 mA/cm^2, respectively (Fig. 5d), the Tafel slope is 44 mV/dec, and the electrochemical activity can be maintained for 20 h, indicating that the catalyst has a stable performance when applied to HER. The excellent catalytic performance of the CoP nanosheet catalysts, as calculated by DFT, is primarily attributable to its ultrathin porous structure with abundant active sites.

In Section 3.5 on crystal phase/crystal plane, the intrinsic activity of TMPs can be modified by changing the phases of the metal phosphides. The preparation of single-crystal phase metal phosphide allows for the investigation of the effect of the preferred

Table 2
Performance comparison and "Stimulatory factors" of HER catalysts with different improvement strategies.

Optimization method	Material (representative)	Overpotential (mV) (@10 mA/cm^2)	Tafel slope (mV/dec)	Electrolyte	Ref.	"Stimulatory factors"
Heteroatom doping	Mn–CoP	100	53	1 mol/L KOH	[22]	Increased conductivity
	V–CoP/CC	98	64	1 mol/L KOH	[23]	New electronic structure lowers reaction energy
	$Co_{2.90}B_{0.73}P_{0.27}$/NF	42	42.1	1 mol/L KOH	[27]	barrier
Morphology and structure control	CoP (hollow polyhedral)	159	59	1 mol/L KOH	[36]	More active sites
		56	43.6	0.5 mol/L H_2SO_4	[41]	Easier material transfer
	S-Ni_5P_4NPA/CP	127	58	0.5 mol/L H_2SO_4	[43]	
	CoP@3D-NPC					
Heterojunction effect	CoP/MoS_2–CNTs	12	42	0.5 mol/L H_2SO_4	[47]	New electronic structure increases conductivity
	CoP_3/$NiMoO_4$–NF	92	79.1	1 mol/L KOH	[48]	Accelerates H* adsorption/desorption
	CoP(MoP)-CoMoO@CN	198	95	1 mol/L KOH	[51]	
Effect of vacancy defect	Vc–FeP	65	62	0.5 mol/L H_2SO_4	[57]	Increase the number of active sites
	V–$Ni_{12}P_5$	27.7	30.88	1 mol/L KOH	[58]	Reduce the adsorption energy of H*
	DR-MoP	104	50	1 mol/L KOH	[59]	
Effect of crystal phase/crystal plane	CoP/NWs	244 (@100 mA/cm^2)	78	1 mol/L KOH	[65]	Unsaturated bonds can act as reaction sites
	$(Fe_xNi_{1-x})_2P$	90	82.7	1 mol/L PBS	[66]	High crystal face index crystals have good
	CoP	56	44	0.5 mol/L H_2SO_4	[67]	stability

crystal surface on the catalytic performance; the amorphous phase metal phosphide is simple to use as the adsorption and desorption sites of the intermediate product owing to the large number of unsaturated bonds in the crystal. Thus, it demonstrates excellent catalytic performance. The atomic structure of the crystal face partially determines the interaction strength between the crystal face and the reactants or reaction intermediates, and the lower the crystal face index, the lower the catalytic activity. The high crystal face index has a high catalytic activity owing to a large number of kinked atoms and edge sites. Furthermore, crystals with a high facet index exist in an environment with short-range order, their atomic structure does not change, and their stability is excellent. Therefore, the catalytic performance can be enhanced by modifying the crystal structure of the catalyst. However, the instability of high-surface-energy crystal faces causes them to rapidly appear and disappear during catalysis. Therefore, the design of high-surface-energy crystal faces with high stability remains challenging.

4. Summary and outlook

TMP-based materials are promising candidates to replace traditional noble metals and their compounds in electrocatalytic hydrogen evolution. Various methods have been developed to prepare TMP-based electrocatalysts, alongside different material engineering strategies. Herein, we have provided a comprehensive summary of these preparation methods and material engineering strategies. To improve the catalytic performance of TMP-based materials for hydrogen production, the following design principles are proposed. (1) Surface structure nanominiaturization. Both the specific surface area and the number of exposed active sites can be increased after nanominiaturization, contributing to the enhancement of the current density per geometric area [68]. (2) More advanced representation. The crystal structure and surface morphology of the samples can be analyzed using advanced *in situ* characterization techniques, including *in situ* X-ray diffraction and *in situ* electron microscopy. Additionally, advanced characterization methods such as HAADF–STEM and XAFS and theoretical calculations (such as DFT) can be used to study the HER reaction mechanism and establish the link between nanomaterials and their properties at the level of the electronic effect [69]. (3) Multifield modulation. During the preparation process of TMPs, multifields, including the magnetic field, thermal field, sound field, and light field, can be used to modify the properties of TMPs. Moreover, these fields can be utilized during the electrocatalysis process to adjust the hydrogen production activities of TMP-based materials. Under the influence of an external field, the motion potential of the electrons in the atomic orbit will change, yielding rapid physical and chemical changes in the material. Multifield modulation is predominately based on the mechanism of free radicals, and HER also contains a substantial number of free radicals. This relationship could provide ideas for multifield modulation [70]. (4) Substrate optimization. Currently, the most popular substrate materials include nickel foam, copper foam, and carbon cloth. The quality of the substrate supporting the electrodes is one of the most important factors affecting their overall performance. Adopting a substrate material with a higher surface area or directly growing 3D TMPs on these supports may be a good way to improve the overall performance of the electrodes [71]. (5) Precise exposure of crystal faces. The introduction of specific exposed crystal pairs is crucial to the performance of catalysts. However, precisely exposing specific crystal planes in the TMPs lattice is a topic worthy of research [72].

With the continued in-depth understanding of the material optimization in TMPs preparation and the reaction mechanisms in hydrogen evolution on these TMP-based electrodes, it is believed that TMP-based materials with superior activities for hydrogen evolution can be designed, and the catalytic performance of TMPs in HER will be gradually enhanced. Hydrogen production *via* water electrolysis on TMP-based electrodes will undoubtedly be realized and contribute to the development of a green and environmentally friendly society (Table 2).

Declaration of competing interest

The authors declare that they have no known competing financial interests or personal relationships that could have appeared to influence the work reported in this paper.

Acknowledgments

We acknowledge support from the National Natural Science Foundation of China (Nos. 22072081, 22002084), and the Fundamental Research Funds for the Central Universities (Nos. GK202201003, GK2021103111).

References

[1] C. Yang, R. Zhao, H. Xiang, et al., Adv. Eng. Mater. 10 (2020) 2002260.
[2] L. Zheng, W. Zhang, B. Gao, et al., Mater. Today Energy 19 (2021) 100600.

[3] H. Jin, Q. Gu, B. Chen, et al., Chem 6 (2020) 2382–2394.
[4] M. Kim, B. Lee, H. Ju, S.W. Lee, J. Kim, Adv. Mater. 31 (2019) 1901977.
[5] X. Zhao, Z. Xue, W. Chen, Y. Wang, T. Mu, ChemSusChem 13 (2020) 2038–2042.
[6] Y. Shi, B. Zhang, Chem. Soc. Rev. 45 (2016) 1529–1541.
[7] H. Zhang, D.H. Ha, R. Hovden, L.F. Kourkoutis, R.D. Robinson, Nano Lett. 11 (2011) 188–197.
[8] B. Du, Z. Cao, Z. Li, et al., Langmuir 25 (2009) 12367–12373.
[9] X. Zheng, S. Yuan, Z. Tian, et al., Chem. Mater. 21 (2009) 4839–4845.
[10] Y. Pan, W. Hu, D. Liu, Y. Liu, C. Liu, J. Mater. Chem. 3 (2015) 13087–13094.
[11] E.J. Popczun, C.G. Read, C.W. Roske, N.S. Lewis, R.E. Schaak, Angew. Chem. Int. Ed. 53 (2014) 5427–5430.
[12] Y. Xu, R. Wu, J. Zhang, Y. Shi, B. Zhang, Chem. Commun. 49 (2013) 6656–6658.
[13] J. Duan, S. Chen, C. Zhao, ACS Appl. Mater. Interfaces 10 (2018) 30029–30034.
[14] Y. Men, P. Li, J. Zhou, et al., ACS Catal. 9 (2019) 3744–3752.
[15] Y. Pei, H. Zhang, L. Han, et al., Nanotechnology 32 (2021) 024001.
[16] J. Wu, X. Ge, Z. Li, D. Cao, J. Xiao, Electrochim. Acta 252 (2017) 101–108.
[17] C.H. Choi, M. Kim, H.C. Kwon, et al., Nat. Commun. 7 (2016) 10922.
[18] N. Bai, Q. Li, D. Mao, D. Li, H. Dong, ACS Appl. Mater. Interfaces 8 (2016) 29400–29407.
[19] Y.Y. Ma, C.X. Wu, X.J. Feng, et al., Energy Environ. Sci. 10 (2017) 788–798.
[20] X.F. Lu, L. Yu, X.W. Lou, Sci. Adv. 5 (2019) eaav6009.
[21] X. Wang, Z. Na, D. Yin, et al., ACS Nano 12 (2018) 12238–12246.
[22] Y. Ge, J. Chen, H. Chu, et al., ACS Sustain. Chem. Eng. 6 (2018) 15162–15169.
[23] W. Hua, H. Sun, L. Ren, D. Nan, Front. Chem. 8 (2020).
[24] M. Ma, G. Zhu, F. Xie, et al., ChemSusChem 10 (2017) 3188–3192.
[25] X. Wang, Y. Chen, B. Yu, et al., Small 15 (2019) 1902613.
[26] D. Wang, T. Liu, J. Wang, Z. Wu, Carbon 139 (2018) 845–852.
[27] H. Sun, X. Xu, Z. Yan, et al., J. Mater. Chem. A 6 (2018) 22062–22069.
[28] Q. Liu, J. Tian, W. Cui, et al., Angew. Chem. Int. Ed. 53 (2014) 6710–6714.
[29] C. Huang, J. Zhou, D. Duan, et al., Chin. J. Catal. 43 (2022) 2091–2110.
[30] F. Ye, Y. Yang, P. Liu, et al., Electrochim. Acta 423 (2022) 140578.
[31] Y. Du, Z. Wang, H. Li, et al., Int. J. Hydrogen Energy 44 (2019) 19978–19985.
[32] X. Yang, A.Y. Lu, Y. Zhu, et al., Nano Energy 15 (2015) 634–641.
[33] A. Sumboja, T. An, H.Y. Goh, et al., ACS Appl. Mater. Interfaces 10 (2018) 15673–15680.
[34] H. Yang, Y. Zhang, F. Hu, Q. Wang, Nano Lett. 15 (2015) 7616–7620.
[35] X. Chen, M. Cheng, D. Chen, R. Wang, ACS Appl. Mater. Interfaces 8 (2016) 3892–3900.
[36] M. Liu, J. Li, ACS Appl. Mater. Interfaces 8 (2016) 2158–2165.
[37] L. Su, X. Cui, T. He, et al., Chem. Sci. 10 (2019) 2019–2024.
[38] C. Tan, X. Cao, X.J. W.u, et al., Chem. Rev. 117 (2017) 6225–6331.
[39] K.H. Liu, H.X. Zhong, S.J. Li, et al., Prog. Mater Sci. 92 (2018) 64–111.
[40] C. Wu, X. Wang, W. Pei, et al., Nanoscale 11 (2019) 15023–15028.
[41] J. Chang, K. Li, Z. Wu, et al., ACS Appl. Mater. Interfaces 10 (2018) 26303–26311.
[42] W. Wei, H. Li, W. Sun, et al., J. Mater. Sci.: Mater. Electron. 31 (2020) 13521–13530.
[43] S. Yang, L. Chen, W. Wei, X. Lv, J. Xie, Appl. Surf. Sci. 476 (2019) 749–756.
[44] C. Liu, T. Gong, J. Zhang, et al., Appl. Catal. B 262 (2020) 118245.
[45] R. Boppella, J. Tan, W. Yang, J. Moon, Adv. Funct. Mater. 29 (2019) 1807976.
[46] Y. Ge, H. Chu, J. Chen, et al., ACS Sustain. Chem. Eng. 7 (2019) 10105–10111.
[47] Y. Pan, Y. Lin, Y. Liu, C. Liu, Catal. Sci. Technol. 6 (2016) 1611–1615.
[48] Y.Q. W.ang, L. Zhao, X.L. S.ui, D.M. G.u, Z.B. W.ang, Ceram. Int. 45 (2019) 17128–17136.
[49] L. Wu, L. Yu, F. Zhang, et al., Adv. Funct. Mater. 31 (2021) 2006484.
[50] W. Mai, Q. Cui, Z. Zhang, et al., ACS Appl. Energy Mater. 3 (2020) 8075–8085.
[51] L. Yu, Y. Xiao, C. Luan, et al., ACS Appl. Mater. Interfaces 11 (2019) 6890–6899.
[52] Y. Wang, B. Kong, D. Zhao, H. Wang, C. Selomulya, Nano Today 15 (2017) 26–55.
[53] X. Huang, Z. Liu, M.M. M.illet, et al., ACS Nano 12 (2018) 7197–7205.
[54] J. Guo, S. Zhang, M. Zheng, et al., Int. J. Hydrogen Energy 45 (2020) 32402–32412.
[55] W. Xie, Z. Li, M. Shao, M. Wei, Front. Chem. Sci. Eng. 12 (2018) 537–554.
[56] W.Z. Zhang, G.Y. Chen, J. Zhao, et al., J. Colloid Interface Sci. 561 (2020) 638–646.
[57] W.L. Kwong, E. Gracia-Espino, C.C. Lee, et al., ChemSusChem 10 (2017) 4544–4551.
[58] J. Duan, S. Chen, C.A. Ortíz-Ledón, M. Jaroniec, S.Z. Q.iao, Angew. Chem. Int. Ed. 59 (2020) 8181–8186.
[59] X. Zhang, Z. Wu, D. Wang, Electrochim. Acta 281 (2018) 540–548.
[60] Z. Wang, S. Wang, L. Ma, et al., Small 17 (2021) 2006770.
[61] J. Lin, Y. Yan, T. Liu, et al., Int. J. Hydrogen Energy 45 (2020) 16161–16168.
[62] Z. Ran, C. Shu, Z. Hou, et al., Chem. Eng. J. 413 (2021) 127404.
[63] Y. Wang, J. Zhang, Front. Chem. Sci. Eng. 12 (2018) 838–854.
[64] W. Liu, J. Shen, Q. Liu, X. Yang, H. Tang, Appl. Surf. Sci. 462 (2018) 822–830.
[65] W. Li, X. Gao, D. Xiong, et al., Chem. Sci. 8 (2017) 2952–2958.
[66] W. Zhang, Y. Zou, H. Liu, et al., Nano Energy 56 (2019) 813–822.
[67] C. Zhang, Y. Huang, Y. Yu, et al., Chem. Sci. 8 (2017) 2769–2775.
[68] X. Yan, Y. Zhao, J. Biemolt, et al., J. Mater. Chem. A 8 (2020) 7626–7632.
[69] C. Sun, H. Wang, J. Ren, X. Wang, R. Wang, Nanoscale 13 (2021) 13703–13708.
[70] S.A. Grigoriev, V.N. Fateev, D.G. Bessarabov, P. Millet, Int. J. Hydrogen Energy 45 (2020) 26036–26058.
[71] N. Mahmood, Y. Yao, J.W. Zhang, et al., Adv. Sci. 5 (2018) 1700464.
[72] J.F. Callejas, J.M. McEnaney, C.G. Read, et al., ACS Nano 8 (2014) 11101–11107.